Science Translational Medicine
AAAS

www.sciencetranslationalmedicine.org/cgi/content/full/9/387/eaah6518/DC1

# Supplementary Materials for

## Bone CLARITY: Clearing, imaging, and computational analysis of osteoprogenitors within intact bone marrow

Alon Greenbaum, Ken Y. Chan, Tatyana Dobreva, David Brown, Deepak H. Balani, Rogely Boyce, Henry M. Kronenberg, Helen J. McBride, Viviana Gradinaru*

*Corresponding author. Email: viviana@caltech.edu

Published 26 April 2017, *Sci. Transl. Med.* **9**, eaah6518 (2017)
DOI: 10.1126/scitranslmed.aah6518

**The PDF file includes:**



**Other Supplementary Material for this manuscript includes the following:**
(available at
www.sciencetranslationalmedicine.org/cgi/content/full/9/387/eaah6518/DC1)

Design file for the chamber holder (.stl)
Raw data values for cell counts (.xlsx)

## Methods

*Computational pipeline:* LSFM generates multidimensional datasets on the order of hundreds of gigabytes, for example 500 GB for tibia with 2 color channels, motivating a necessity for high-throughput automated computational tools to do data processing, management, and visualization. Thus, we established a computational pipeline optimized for large datasets that interfaces between 3D visualization and analysis software (Imaris, Bitplane) and a programming framework (Matlab, Mathworks) although alternatives can also be used (e.g. Amira, Python).

Tile stitching was done with TeraStitcher (49). The acquired tiles (.tiff format) were saved according to the TeraStitcher two-level hierarchy and file naming convention. The resulting stitched tiles were saved as large individual.tiff format file per Z section. To accelerate processing and manipulation of 3D images in Imaris, the lateral resolution was down-sampled by a factor of 2 and 4 for vertebrae and long bones, respectively. These image stacks were then converted into a single large multiresolution 3D Imaris image. The 3D image is then used to construct the VOI, performing quality control for the automatic cell detector, and obtaining relevant statistics about the position of the cells within the VOI.

Using Imaris surface tools, a VOI was constructed around the bone surface, while excluding connective tissue. The VOI was used to count cells and evaluate morphology (fig. S7). For the femur and tibia, the VOI was defined around known anatomical regions: the third trochanter and tibial crest, respectively. The surface for the vertebral body aimed to surround the inner marrow of interest and exclude surrounding compact bone and chondrocyte-dense endplates.

2D stitched images were used for automatic $Sox9^+$ cell detection (Fig. 2B). The algorithm iterates through the image stack and divides the 2D stitched images into a number of smaller regions. For each region, the standard deviation and mean value of fluorescence intensity is calculated. $Sox9^+$ cells are expected to be significantly brighter in intensity than the surrounding tissue, therefore each sub region is thresholded with a value of approximately 9 standard deviations above the mean value. The thresholded images are then converted to a binary format and morphological operations are conducted to improve connectivity and discard noise. A 3D binary matrix is then constructed from the 2D binary images and connected voxels are grouped into 3D blobs. Blobs that showed one of the following criteria were removed: (i) blobs with volume outside of a 523-33,500 $\mu m^3$ range, (ii) blob with spatial position outside of the VOI and (iii) blobs that show strong signal in the autofluorescence channel. The centroids of the remaining blobs are imported into Imaris to perform manual adjustments. The goal of the automatic detection is to facilitate manual detection by saving time and reducing the chance of error from long annotation sessions.

Using Imaris' clipping plane tool, the 3D image is divided into thick slices (~ 100 μm) to allow for manual adjustments of the automatically detected cells. Viewing cells in these thick

sections allows for visualization of 3D features that help to accurately identify cells. When counting the cells, 2 color channels were used to disambiguate between autofluorescence (green) and the true $Sox9^+$ signal (red). If the $Sox9^+$ cell under question is present with strong intensity in the autofluorescence channel, then it was not included in the quantification.

Following manual cell count adjustments, Imaris was used to generate distance to surface and cell count statistics. The surface was imported into Imaris' cell object with the marked $Sox9^+$ spots as its vesicles. Automatically generated statistics were imported to Matlab for further processing and plotting.

*Sample mounting for light-sheet microscope:* To mount the sample for LSFM, one end of a 4 cm long plastic capillary was flattened using a plier, and a small amount of All Purpose Krazy Glue (KG585) was applied on this end. The flattened end was later placed on the edge of the cleared condyles (femur) and L3 (vertebral column) bone while moderate pressure was applied. Four minutes later, the capillary bonded with the bone and the sample was placed back into RIMS. Before imaging, the plastic capillary was fitted to a glass capillary, which can be attached to the sample stage of the LSFM (fig. S5).

*Simulated stereology:* To investigate the variability between 3D counting and 2D section counting, we performed a series of simulated stereology experiments using our 3D datasets. To start, the coordinates of each cell center were imported to MATLAB as a list, and the VOI was imported to MATLAB as a binary mask. From the binary mask, the volume of each 2D section was calculated by accumulating the number of pixels in the 2D section and multiplying it by the voxel size. Then, a simple random sampling stereology experiment was simulated by stochastically selecting $N$ digital sections (6 μm thick) from the entire VOI. Only cells whose centroids were within the volume of the selected digital sections were counted, this guarantees that each cell will be counted only once and cell will not be overrepresented. To calculate the cell density, the total number of counted cells in the selected digital sections was divided by their accumulated volume. From sampled cell density and the known volume of the entire bone, the total number of cells in the bone was estimated. In order to calculate the coefficient of variation, each experiment was repeated 5 times and the standard deviation of the experiments was divided by the total cell number of the volume. To reflect modern stereology sampling techniques, we also simulated systematic uniform random sampling (SURS) stereology experiments. As compared to simple random sampling, SURS has a stricter subset of possible samplings. Rather than looking at any random subset of slices, SURS requires sampling the tissue with a fixed interval, while the first starting slice is randomly selected (Fig. 3A). In order to compare SURS with simple random sampling, each SURS experiment consisted of a specific number of digital slices. Since a specific number of digital slices can be attained by a variety of sample intervals, the minimum interval that would yield the desired number of slices was selected. Once the digital sections were selected for SURS, the cell density was calculated in the same manner as simple random sampling. To calculate the coefficient of variation, each SURS experiment was

repeated for 5 random starting positions. Figure 3C shows only numbers of slices that yielded at least 5 possible starting positions.

*Quantifying the effect of amino alcohol (related to fig. S2):* High levels of autofluorescence can overshadow elements of interest and lead to false inclusion of features. Intensity data from the mouse femur and tibia before and after treatment with amino alcohol (N,N,N',N'-tetrakis(2-hydroxypropyl) ethylenediamine) (Sigma, #122262-1L) were analyzed. The starting depth (0 µm) was defined as the first section that contained both sufficient compact bone and marrow for analysis. Then, for 7-9 depths along the imaging dimension, two areas (~ 1000 $\mu m^2$) were extracted. The first area exclusively contained compact bone, while the other exclusively contained marrow. The mean intensities of the two areas (marrow and compact bone) were then calculated. The mean intensity ratio (marrow versus compact bone) was used to quantify the amino alcohol effect on quenching auto-fluorescence in the marrow, since amino alcohol operates on heme, which is found only in the marrow. To verify that amino alcohol did not quench endogenous fluorescence, we compared the same region of the bone before and after amino alcohol treatment (fig. S2).

*Quantifying imaging depth at different anatomical regions of the bone (related to fig. S6):* Bone tissue is difficult to clear and image in 3D, particularly in deeper regions where the SNR is low. Additionally, bones are highly heterogeneous and different regions have significantly different biological makeup that affects imaging SNR. In order to characterize the imaging depth capabilities of LSFM in bone tissue cleared by Bone CLARITY, we quantitatively assessed cell detection in several anatomically distinct regions using a Peak SNR (PSNR) metric (equation 1).

$$PSNR = 20 \times \log_{10} \frac{MAX-\mu}{\sigma} \quad (1)$$

MAX is the maximum intensity of pixels in the region containing the cell, µ is the mean intensity of all pixels in the region that is at least 20 µm away from the cell center, and σ is their standard deviation. For each anatomical region, the starting point (0 µm) of the sample was defined as the first depth that bone tissue filled at least 50% of the field-of-view. Then, at least 10 isolated $Sox9^+$ cells were selected along the image stack and their PSNR were calculated. For PSNR calculation, an area of 0.123 $mm^2$ and 0.086 $mm^2$ (for long bones and vertebrae, respectively) was used for the region around the cell. Based on visual inspection, the minimum PSNR for cell detection was 24. Consequently, we could reliably image bone tissue to a depth of approximately 1.5 mm. With the exception of chondrocyte-dense regions such as the growth plate and the epiphysis, this demonstrates that Bone CLARITY and LSFM provide end-to-end imaging of mouse bone tissue. Note that in regions with high concentration of chondrocytes, no isolated cells could be found, thus creating large gaps along the imaging depth in fig. S6E.

*Antibody staining:* Mice were perfused transcardially with 0.01M PBS (Sigma, #P3813) followed by 4% paraformaldehyde (PFA) (VWR, #100496-496). The femurs and tibias were

extracted and post-fixed overnight with 4% PFA. The bones were demineralized with 10% EDTA in 0.01M PBS (Lonza, #51234) for two weeks at 4 degrees with daily solution exchange. Afterwards, the bones were incubated in 30% sucrose (Sigma, #S0389) in 0.01M PBS until they equilibrated to the solution. Next, the bones were embedded in OCT compound (Sakura Finetek, #M71484) in a tissue mold cassette and slowly frozen in powdered dry ice containing ethanol (Sigma, #E7023). The bones were then cut along its longitudinal plane with a cryostat (Leica, Biosystems) until one-half remained. The OCT compound was removed from the bisected bone and cleared following the Bone CLARITY protocol starting with hydrogel embedding and ending before refractive index matching stage. Antibody staining was performed using an anti-osteocalcin antibody (Abcam, #ab93876) at 1:100 in 0.5mM SDS with 0.01 % sodium azide (Ricca Chemical Company, #7144.8-16) for 2 days at room temperature. The bones were then washed for 2 days at room temperature using PBST (0.02% Triton-X100) and then incubated in secondary conjugated to Alexa-647 (Jackson Immuno Research, #711-606-152) for 2 days. Samples were then washed for 2 days and incubated in RIMS stepwise from 1.38-1.47 over 3 days. Bones were then imaged using a Zeiss 780 confocal.

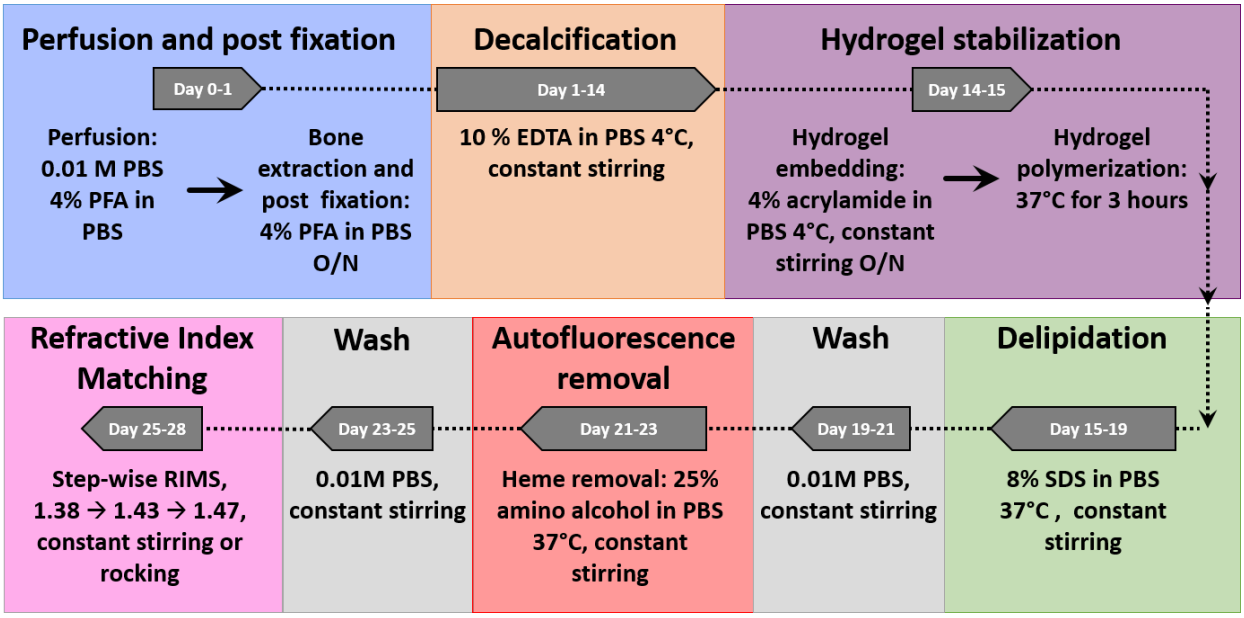


**Fig. S1. Bone CLARITY clearing process.** (**A**) As a first step (blue) in Bone CLARITY method transcardial perfusion is performed with 0.01M PBS, pH 7.4, and 4% paraformaldehyde (PFA) in PBS, pH 7.4. Hard tissue is then extracted and post-fixed with 4% PFA in PBS, pH 7.4 at 4°C for 16 hours. Hard tissue is then decalcified (orange). During this step, daily-exchange of 10% EDTA in PBS, pH 8, at 4°C under constant stirring is performed. Hydrogel stabilization to prevent protein loss is carried out (purple). The tissue is incubated in a hydrogel composed of 4% acrylamide with 0.25% VA044 in PBS at 4°C under constant stirring for 16 hours. Afterwards, the hydrogel is degased with nitrogen gas and polymerized at 37°C. Delipidation is carried out with 8% SDS in PBS, pH 7.4 at 37°C under constant stirring (green). A wash step with PBS is performed before heme removal from the tissue (gray). Heme removal is performed with 25% amino alcohol in PBS, pH 9, at 37°C under constant stirring (red). A second wash step is performed on the tissue (gray). Finally, the tissue is refractive index matched to 1.47 through daily step-wise buffer exchange (pink).

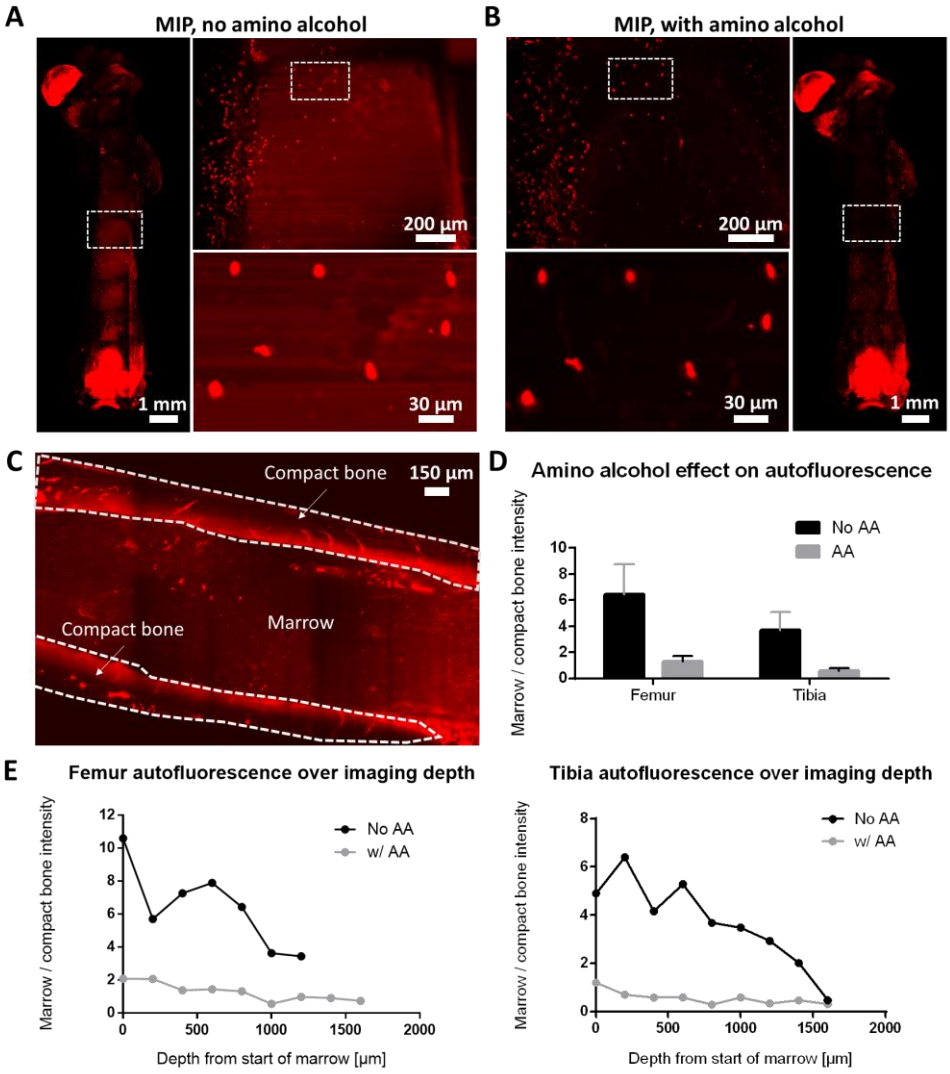


**Fig. S2. The effect of amino alcohol on reducing autofluorescence.** (**A**) MIP of a mouse femur rendered transparent using Bone CLARITY without the addition of amino alcohol. The dashed regions show the locations of progressively zoomed in images. (**B**) MIP of the same mouse femur shown in (A), after the addition of amino alcohol. Zoomed in images of the same regions as in (A) show that the same spatial pattern in the sample was maintained after amino alcohol treatment. (**C**) A representative image of the regions of tissue (marrow and compact bone) used for the analysis of the autofluorescence quenching effect. (**D**) The mean ratio of marrow to compact bone intensity in a mouse femur and tibia before and after the addition of amino alcohol - which removes autofluorescence in the bone marrow. The intensity ratio between the marrow and compact bone should be independent of the imaging depth and illumination variations. (**E**) The ratio of marrow to compact bone intensity from different sample regions along the imaging depth of the bone. A depth of 0 µm refers to the first region along the imaging depth that had both marrow and compact bone.

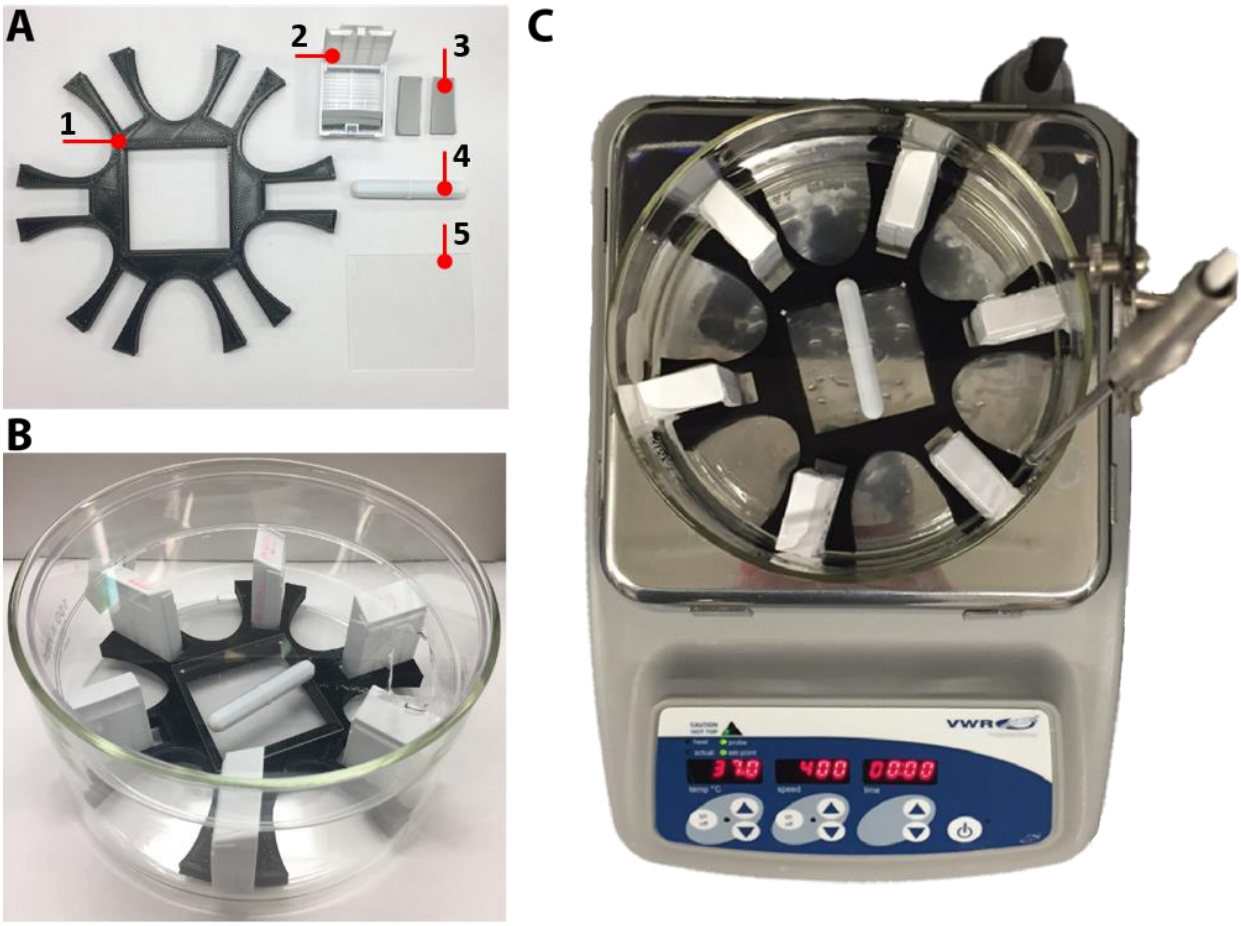


**Fig. S3. Bone CLARITY setup.** (**A**) The individual parts of the setup, which is composed of: (1) A 3D printed holder for histology cassettes. (2) A large histology cassette with rubber inserts. (3) Rubber inserts to prop the tissue above the 3D printed holder, and consequently position the tissue within the convective current. (4) A stir bar. (5) A glass slide for placement of the stir bar above the 3D printed holder. (**B**) The histology cassettes arranged inside a 15 cm petri dish with a 14.7 cm plastic petri dish cover. (**C**) The petri dish is placed on a closed loop temperature controlled stir plate. For repeatability, six cassettes are always placed in the chamber, and the stir bar is rotated at a speed of 400 rotations per minute at 37ºC. The design file for the 3D printed holder is available as an auxiliary supplementary file.

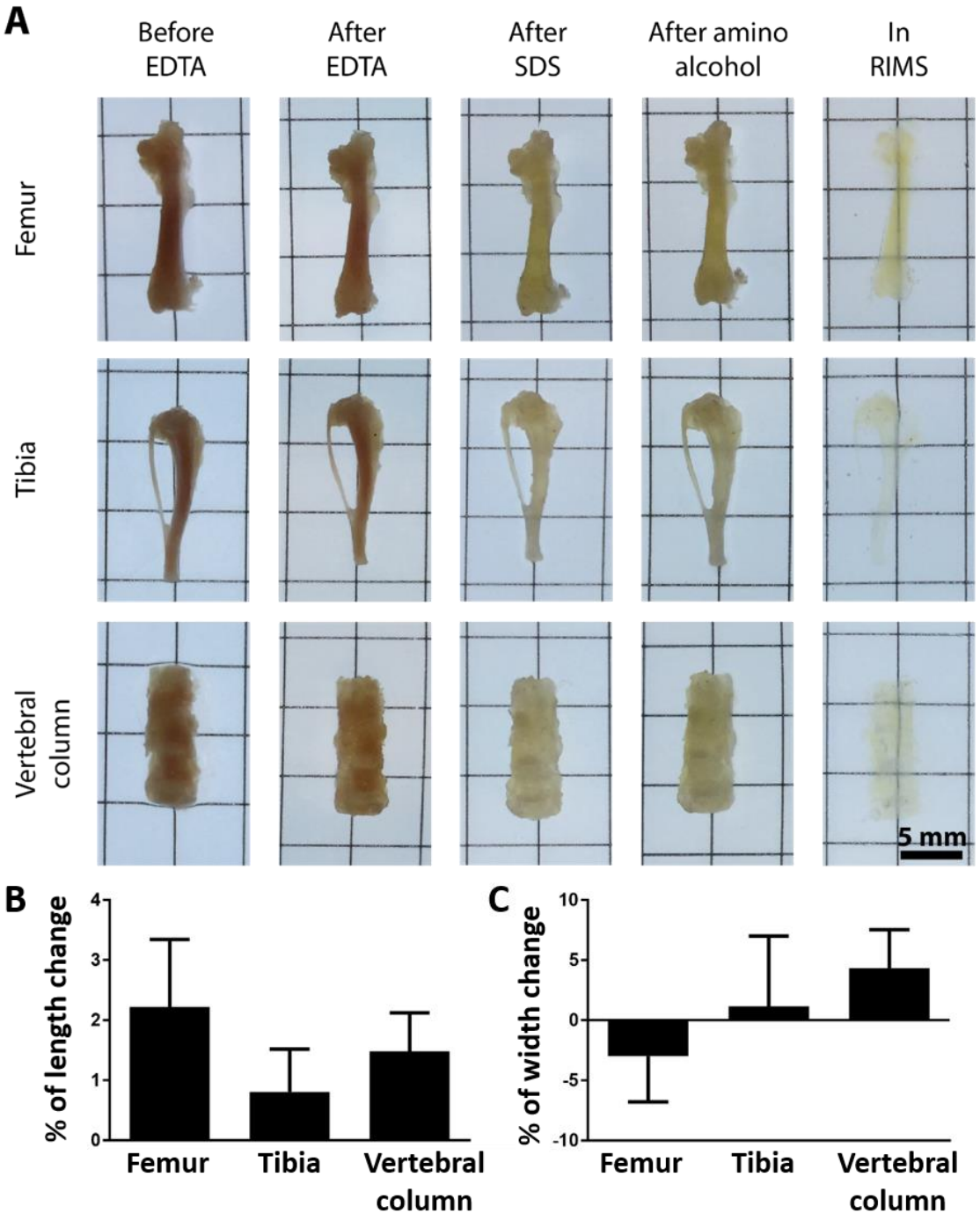


**Fig. S4. Sample progression through Bone CLARITY clearing process.** (**A**) Micrographs documenting the progression of the femur, tibia and vertebral column throughout each phase of Bone CLARITY. (**B**) The percent change in length of the bones before and after Bone CLARITY. (**C**) The percent change in width of the bones before and after Bone CLARITY. For (B) and (C), n = 6 for the femur, n = 5 for the tibia and n = 4 for the vertebral column. All values are mean ± s.e.m.

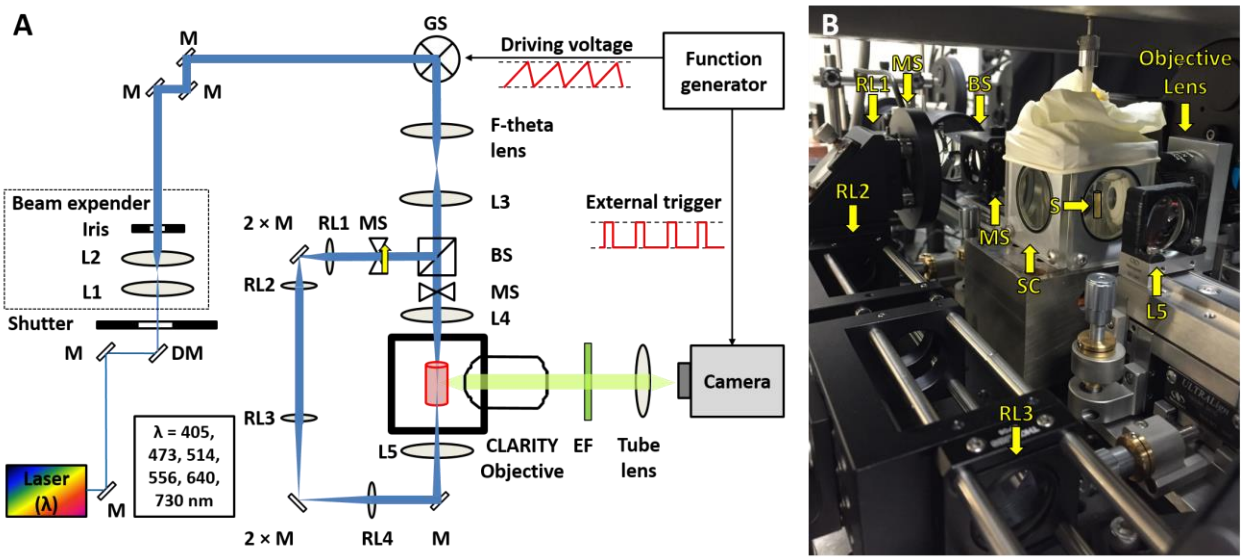


**Fig. S5. LSFM setup.** (**A**) Schematic diagram of the multi-color dual-side illumination light-sheet microscope with the confocal slit detection. The microscope acquisition speed is up to 22 frames per second; consequently, it allows for high-resolution acquisition of large cleared tissue. L – lens, M – mirror, DM - dichroic mirror, GS – galvano scanner, BS – beam splitter, MS – mechanical shutter, RL – relay lenses and EF emission filter. (**B**) A photograph of the light-sheet setup, the sample (S) is directly immersed in the sample chamber (SC).

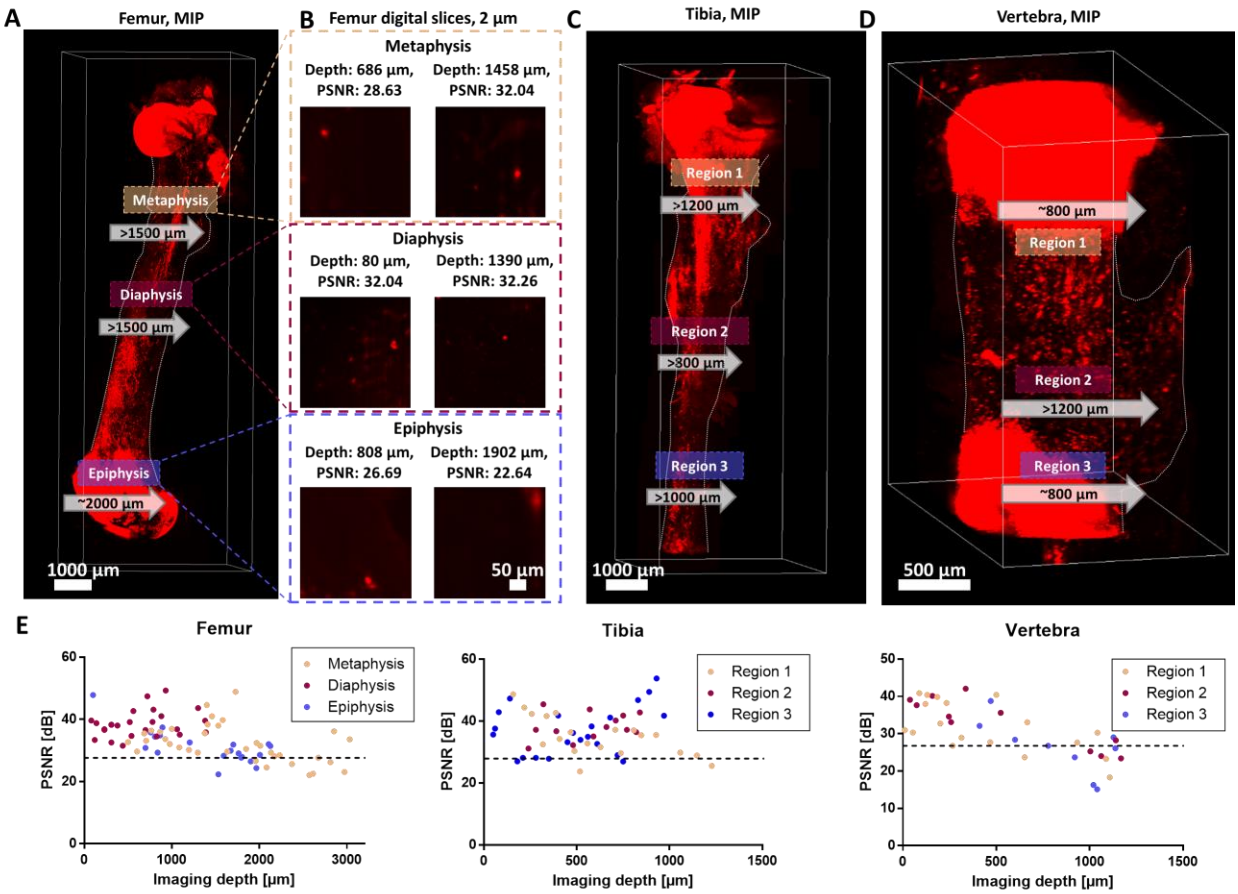


**Fig. S6. Signal quality metrics to quantify imaging depth of Bone CLARITY.** (**A**) MIP of a cleared mouse femur with estimates of imaging depth limit at different anatomical regions. The arrows indicate the direction of analysis and the calculated imaging depth. (**B**) Examples of isolated Sox9$^+$ cells at different imaging depths and in different bone regions. Sox9$^+$ cells remain distinguishable at the deepest parts of the metaphysis and diaphysis, but signal loss is evident in the deeper parts of the epiphysis. The same analysis was repeated for a cleared mouse tibia (**C**) and vertebra (**D**). (**E**) The peak signal-to-noise ratio (PSNR) of isolated Sox9$^+$ cells. The dashed lines represent a qualitative estimate of where cells are no longer distinguishable from background noise, at a PSNR of around 24.

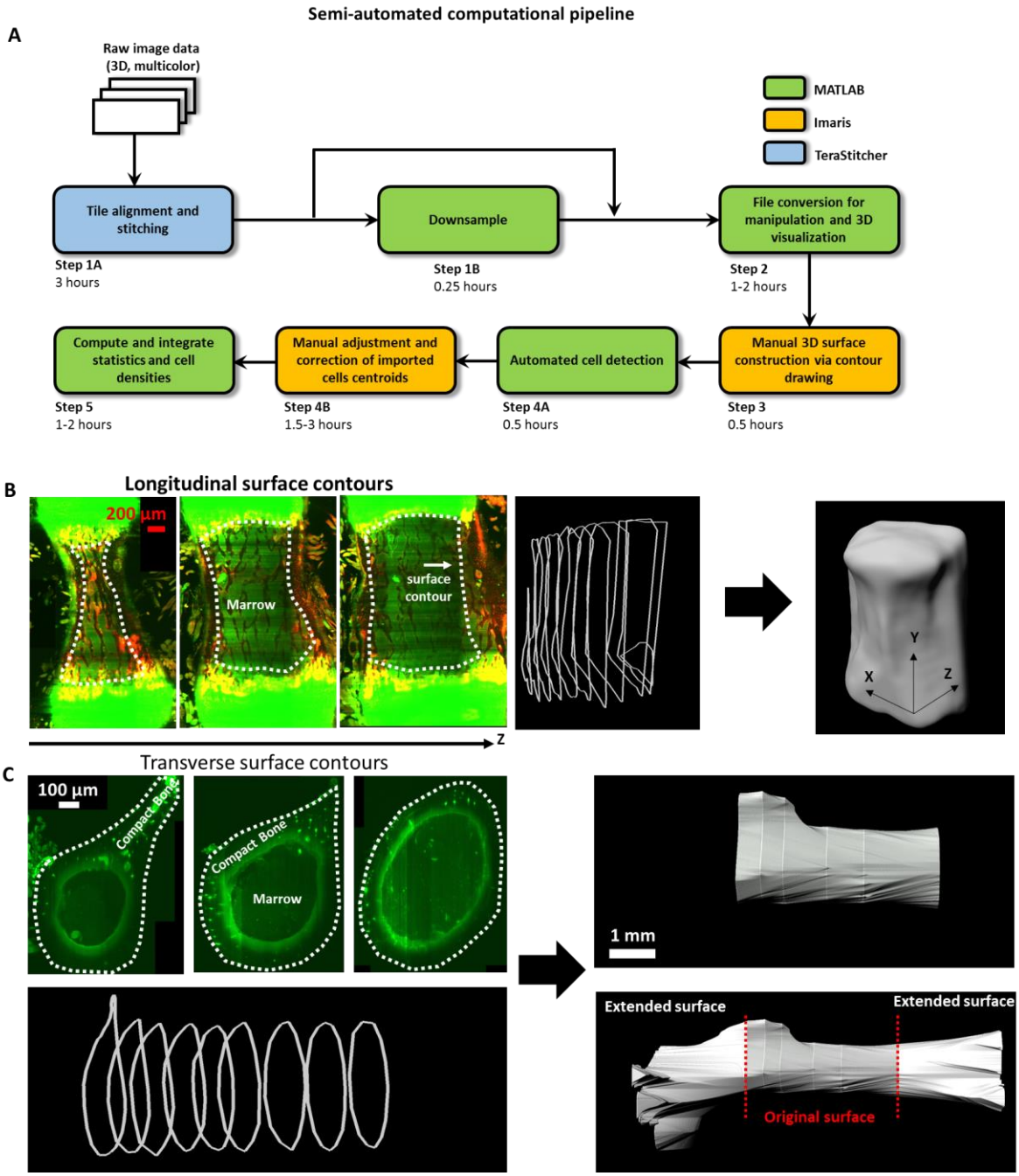


**Fig. S7. Computational pipeline.** (**A**) A block diagram of the computational pipeline. (**B**) VOI creation in the vertebra body. In each block of approximately 10 longitudinal sections a ROI (dotted line) is marked around regions that contain marrow. The VOI is then interpolated from the ROIs. (**C**) VOI creation in the tibia and femur, where approximately 10 transverse slices are used to create the VOI. For cell distance to surface calculation, the VOI is extended from both ends, in order to ensure distance calculation to the real bone boundaries and not to artificial perpendicular surfaces.

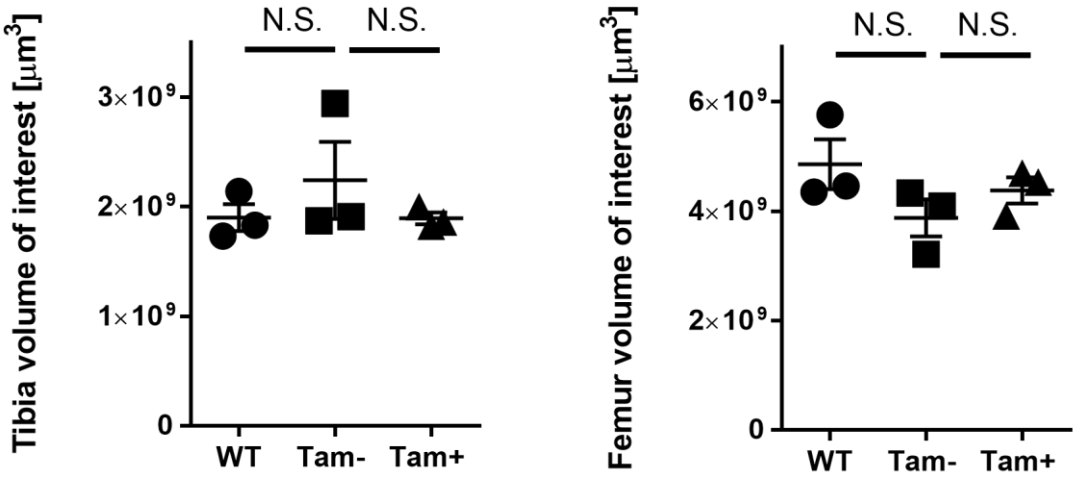


**Fig. S8. Volume comparisons in the tibia and femur.** No significant change in the volume of interest was observed between the $Sox9^{+}$ and $Tam^{+}$ group and the two control groups (wild type; $Sox9^{+}$ and $Tam^{-}$). For all groups n = 3, all values are mean ± s.e.m; two-tailed, unpaired t-test, ($p \geq 0.05$ = N.S.).

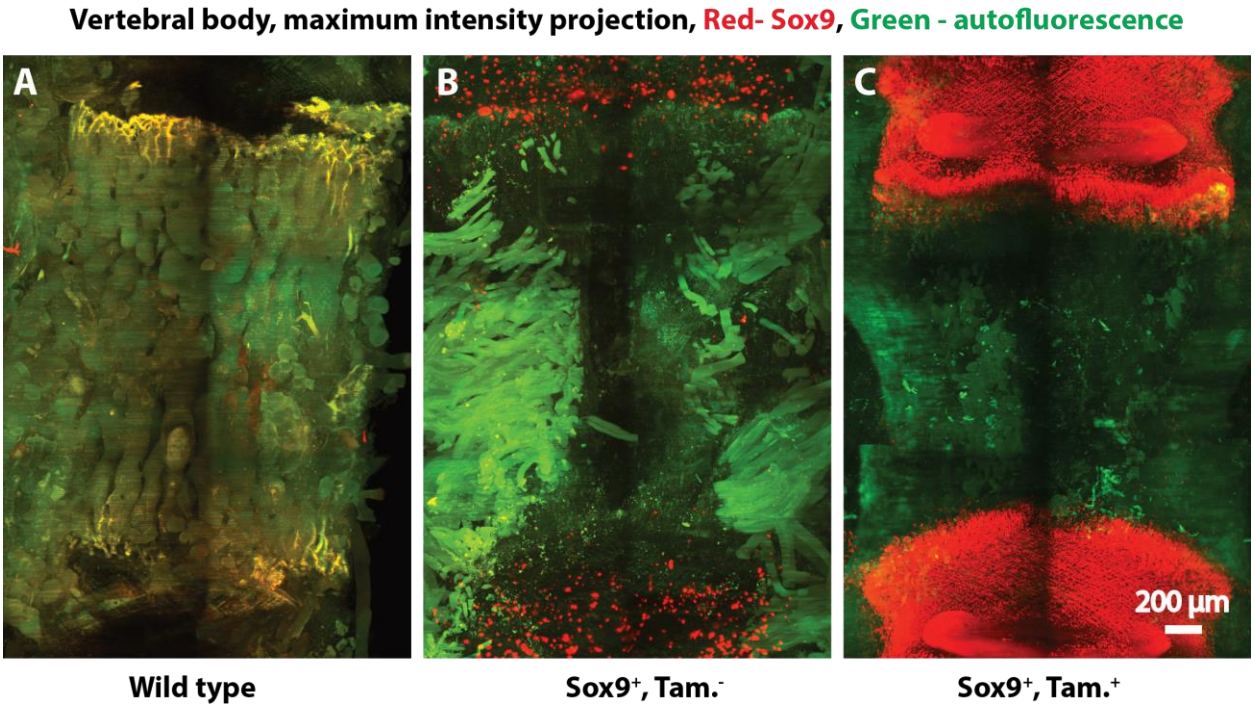


**Fig. S9. tdTomato expression in the vertebral columns.** (**A**) No fluorescence signal is present in the emission spectrum of tdTomato (556 nm laser excitation) in the vertebral column of a wild-type mouse. (**B**) Using the same imaging settings as in panel (A), $Sox9^{+}$ mouse shows tdTomato expression even without tamoxifen induction. The fluorescence signal is primarily located at the endplates and attributed to leakage. (**C**) Using the same imaging settings as panel (A), $Sox9^{+}$ mouse shows high levels of tdTomato expression after tamoxifen induction.

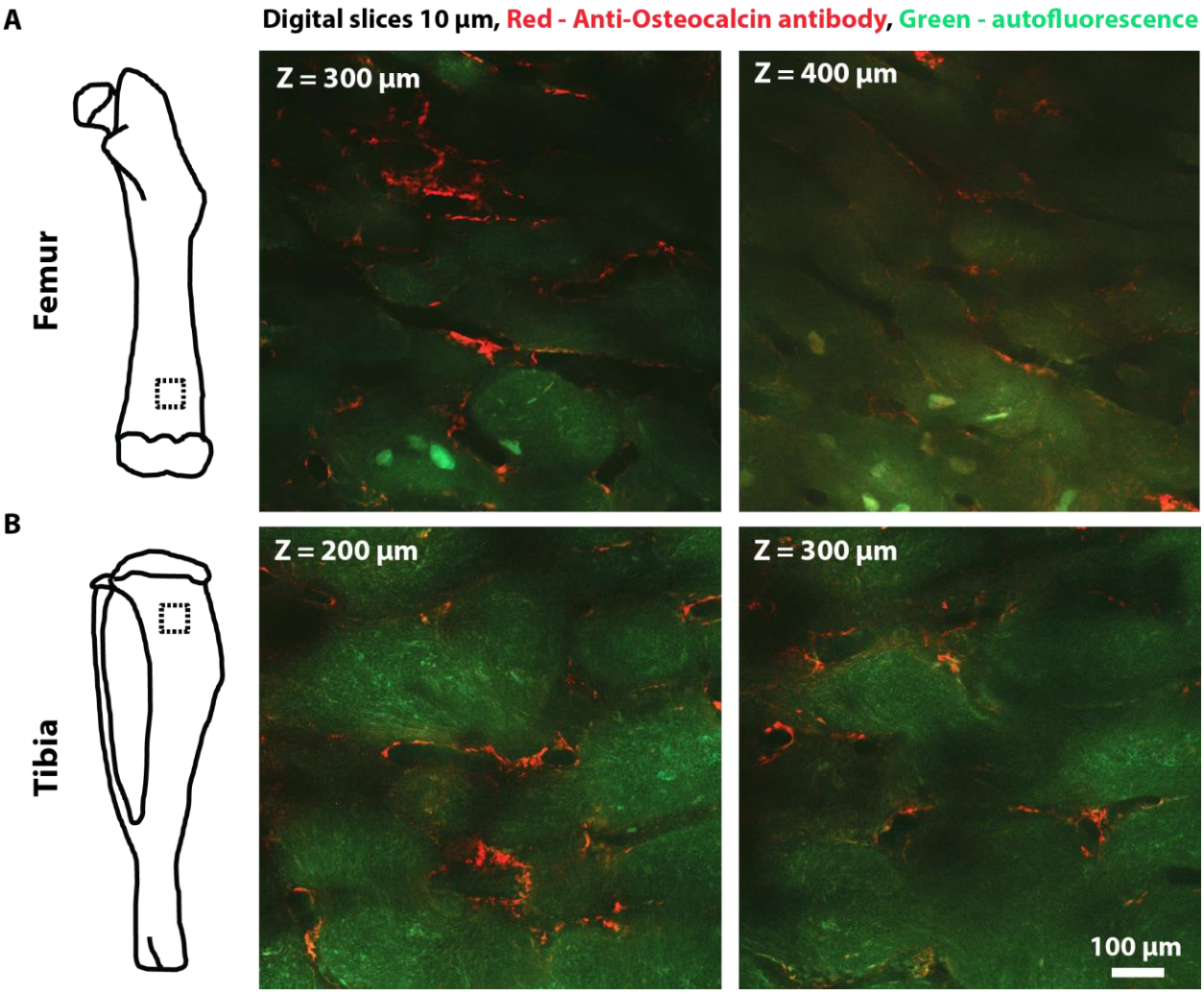


**Fig. S10. Antibody staining using Bone CLARITY.** (**A**) The approximate region imaged in the bisected femur is outlined by a black square. Digital slices of 10 µm thickness are shown in 300 and 400 µm from the surface of the femur. Red shows Osteocalcin staining of cells lining the surface of bone, green shows autofluorescence. (**B**) The region imaged in the bisected tibia is outlined by a black square. Digital slices of 10 µm thickness are shown in 200 and 300 µm from the surface of the tibia. Red shows Osteocalcin staining of cells lining the surface of bone, green shows autofluorescence.

**Movie S1. Visualizing endogenous fluorescence throughout a cleared mouse femur.** The movie shows a MIP image of an entire mouse femur at different angles and zoomed in view of the greater trochanter area. Digital sections with 30 µm thickness are shown at different bone depths at the greater trochanter. $Sox9^+$ cells are labeled with red fluorescent protein (tdTomato), while tissue autofluorescence in green provides structural cues.

**Movie S2. Visualizing endogenous fluorescence throughout a cleared mouse tibia.** MIP image of an entire mouse tibia rotated in different angles. Zoomed in digital sections (30 µm thick) of the tuberosity and the diaphysis are shown. The $Sox9^+$ cells are labeled with tdTomato and tissue autofluorescence in green for structural orientation. When the red channel is turned off (Z = 2016 µm) some cellular processes can be seen.

**Movie S3. Visualizing endogenous fluorescence throughout a cleared mouse vertebral body.** The movie shows an L4 vertebra body of a mouse. The intervertebral disks labeled in red can be seen in the vertical edge of the image. Longitudinal sections (30 µm thick) of the vertebra body at different depths can also be seen where the red channel shows $Sox9^+$ cells and the green channel shows tissue autofluorescence.